

AD-A116 999

MCDONNELL DOUGLAS RESEARCH LABS ST LOUIS MO

F/G 20/7

SHORT-PULSE ELECTRON-BEAM PROPAGATION EXPERIMENTS IN A CONTROLL--ETC(U)

MAR 82 M A GREENSPAN

N60921-81-C-0152

UNCLASSIFIED

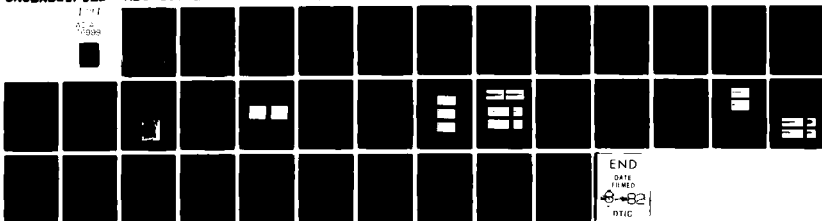
MOC-80762

NL

1-1

1-1

1-1



END
DATE
FILMED
4-82
DTIC

①

**SHORT-PULSE ELECTRON-BEAM
PROPAGATION EXPERIMENTS IN A
CONTROLLED-ENVIRONMENT CHAMBER**

M.A. Greenspan

**McDonnell Douglas Research Laboratories
St. Louis, Missouri 63166**

**Final Technical Report
8 March 1982
for Period 8 June 1981 - 8 March 1982**

Approved for public release; distribution unlimited

**DTIC
ELECTE
JUL 19 1982
S D E**

**Sponsored by
Defense Advanced Research Projects Agency (DoD)
ARPA Order No. 3718/35
Monitored by Naval Surface Weapons Center
under contract N60921-81-C-0152**

DTIC FILE COPY

82 07 19 032

AD A1150

Disclaimer

The views and conclusions contained in this document are those of the author and should not be interpreted as representing the official policies, either expressed or implied, of the Defense Advanced Research Projects Agency of the U.S. Government.

UNCLASSIFIED

SECURITY CLASSIFICATION OF THIS PAGE (When Data Entered)

REPORT DOCUMENTATION PAGE		READ INSTRUCTIONS BEFORE COMPLETING FORM
1. REPORT NUMBER	2. GOVT ACCESSION NO. AD-A116999	3. RECIPIENT'S CATALOG NUMBER
4. TITLE (and Subtitle) SHORT-PULSE ELECTRON-BEAM PROPAGATION EXPERIMENTS IN A CONTROLLED-ENVIRONMENT CHAMBER		5. TYPE OF REPORT & PERIOD COVERED Final Technical Report 8 June 1981 - 8 March 1982
		6. PERFORMING ORG. REPORT NUMBER MDC Q0762
7. AUTHOR(s) M. A. Greenspan		8. CONTRACT OR GRANT NUMBER(s) N60921-81-C-0152
9. PERFORMING ORGANIZATION NAME AND ADDRESS McDonnell Douglas Research Laboratories McDonnell Douglas Corporation St. Louis, MO 63166		10. PROGRAM ELEMENT, PROJECT, TASK AREA & WORK UNIT NUMBERS
11. CONTROLLING OFFICE NAME AND ADDRESS Defense Advanced Research Projects Agency 1400 Wilson Boulevard Arlington, VA 22209		12. REPORT DATE 8 March 1982
		13. NUMBER OF PAGES 33
14. MONITORING AGENCY NAME & ADDRESS (if different from Controlling Office) Naval Surface Weapons Center White Oak Laboratory Silver Springs, MD 20910		15. SECURITY CLASS. (of this report) Unclassified
		15a. DECLASSIFICATION/DOWNGRADING SCHEDULE
16. DISTRIBUTION STATEMENT (of this Report) Approved for public release; distribution unlimited		
17. DISTRIBUTION STATEMENT (of the abstract entered in Block 20, if different from Report)		
18. SUPPLEMENTARY NOTES		
19. KEY WORDS (Continue on reverse side if necessary and identify by block number) Beam propagation Nose erosion Relativistic electron beams Charge return Charged particle beams		
20. ABSTRACT (Continue on reverse side if necessary and identify by block number) → Propagation of a 500-keV, 6-kA, 3-ns electron beam in air has been studied in a 3.4 m diam controlled-environment chamber at pressures of 75-1600 Pa (0.56-12 Torr). Open-shutter photography, Faraday cup, and magnetic-field probe measure- ments were performed, and results were compared with those obtained for beam propagation in a 7.6 cm diam glass tube. Over a propagation window of		

DD FORM 1473
1 JAN 73

EDITION OF 1 NOV 65 IS OBSOLETE

UNCLASSIFIED

SECURITY CLASSIFICATION OF THIS PAGE (When Data Entered)

UNCLASSIFIED

< or APPROX.

SECURITY CLASSIFICATION OF THIS PAGE(When Data Entered)

270-800 Pa, rectilinear propagation to within $\lesssim 5$ mrad was observed despite the lack of guide tube walls. Propagation at the low end of the window was limited by rapid nose-erosion rates of up to 10 cm/ns. At optimal propagation pressures (400-550 Pa), magnetic probe data were used to estimate induced electric fields and nose erosion caused by ohmic energy loss. Results were consistent with Faraday cup and calorimeter data. At higher pressures, propagation was erratic, and appeared to be terminated by the lack of a stable pinch formation. For those shots where propagation was observed at pressures above 550 Pa, Faraday cup traces show a loss of the beam tail.

UNCLASSIFIED

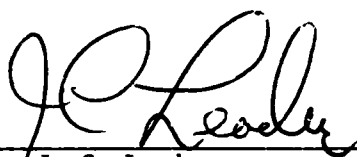
SECURITY CLASSIFICATION OF THIS PAGE(When Data Entered)

PREFACE

This final report is an account of the work completed at the McDonnell Douglas Research Laboratories on Naval Surface Weapons Center Contract No. N60921-81-C-0152, sponsored by Defense Advanced Research Projects Agency ARPA Order No. 3718/35.

The work was conducted in the Radiation Sciences Department, managed by Dr. J. C. Leader. The principal investigator was Dr. M. A. Greenspan. The program monitor was Dr. C. M. Huddleston, Naval Surface Weapons Center.

This report has been reviewed and approved.



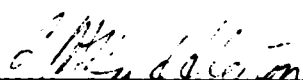
Dr. J. C. Leader
Chief Scientist-Radiation Sciences
McDonnell Douglas Research Laboratories



Dr. D. P. Ames
Staff Vice President
McDonnell Douglas Research Laboratories



Accession For	
NTIS GRA&I	<input checked="checked" type="checkbox"/>
DTIC TAB	<input type="checkbox"/>
Unannounced	<input type="checkbox"/>
Justification	
By	
Distribution/	
Availability Codes	
Dist	Avail and/or Special
A	



Dr. C. M. Huddleston
Naval Surface Weapons Center

TABLE OF CONTENTS

	<u>Page</u>
SUMMARY.....	1
1.0 INTRODUCTION.....	3
2.0 EQUIPMENT.....	4
2.1 Beam Generator.....	4
2.2 Controlled-Environment Chamber.....	4
2.3 Diagnostic Positioners.....	7
3.0 DIAGNOSTICS.....	8
3.1 Signal Acquisition.....	11
3.2 Experimental Results.....	11
4.0 MODEL COMPARISON.....	21
5.0 CONCLUSIONS.....	24
REFERENCES.....	25

LIST OF ILLUSTRATIONS

<u>Figure</u>	<u>Page</u>
1. Febetron electron-beam current, electron-beam energy, and time-integrated radial profile of electron-beam current density.....	5
2. Experimental arrangement for short-pulse electron-beam experiments in a 3.4-m diameter controlled-environment chamber.....	6
3. Remotely controlled B_θ probe positioner installed in MDC controlled-environment chamber.....	7
4. Faraday-cup/calorimeter used in short-pulse relativistic electron-beam experiments.....	8
5. Reed-switch pulser arrangement, pulser output, and Faraday-cup output.....	9
6. Diagram of a magnetic-field probe used in electron-beam experiments, calibration arrangements, and recorded output.....	10
7. Typical open-shutter photographs of propagation in bent guide tubes.....	11
8. Open-shutter photographs of a Febetron 706 electron beam propagating in a controlled-environment chamber showing that the beam position is not affected by movement of the Faraday cup.....	13
9. \dot{B}_θ probes at $z = 120$ cm, pressure = 530 Pa (4 Torr).....	13
10. Energy transfer measured by calorimeter in a controlled-environment chamber.....	14
11. Total charge collected by Faraday cup as a function of pressure in a controlled-environment chamber (solid curves) with drift-tube data (dashed curves) shown for comparison.....	14
12. Time-correlated Faraday-cup traces showing beam-front velocity.....	15
13. Open-shutter photographs at 1070 Pa (8 Torr) showing large shot-to-shot variations.....	17
14. Magnetic-probe data (net current) as a function of radial position..	17
15. Open-shutter photographs of beam propagation at $P = 270$ Pa showing severe perturbation caused by the magnetic-field probes.....	18
16. Topology of net current flow.....	19

LIST OF TABLES

<u>Table</u>	<u>Page</u>
1. Beam Front-Velocity Data.....	16

SUMMARY

The primary objectives of the research program entitled "Short-Pulse Electron-Beam Propagation Study" performed by the McDonnell Douglas Research Laboratories (MDRL) were to (a) study the propagation of a short-pulse relativistic electron beam in an open but controlled environment and (b) compare observed propagation results under open-chamber conditions with propagation results measured in a drift tube.

This research was accomplished using a Febetron 706 electron-beam generator yielding an electron beam having a peak energy of 500 keV with a beam current of 6 kA and a pulse width of 3 ns (FWHM). The primary diagnostics employed for the propagation measurements were (a) open-shutter photography, (b) Faraday cup measurements of beam current, (c) calorimetry measurements of beam energy transport, and (d) magnetic-field probe measurements of net current transport. Measurements were made in air over a pressure range of 75-1600 Pa (0.5-12 Torr) at various axial and radial positions. Over a propagation window of 270-800 Pa, rectilinear propagation to within 5 mrad was observed despite the lack of guide tube walls. Measured open-chamber beam current and total charge transport were greater than in a 7.6 diam drift tube at optimum pressure (400-550 Pa), but less than in the drift tube at lower and higher pressures. Propagation at the low-pressure end of the window was limited by rapid nose-erosion rates of up to 10 cm/ns, as was also observed in the drift tube. At high pressures, propagation was limited by a lack of a stable pinch equilibrium, with losses predominantly at the beam tail. At the optimal propagation pressure (540 Pa), analysis of magnetic-field probe data showed that nose erosion resulting from ohmic-energy loss provided the main energy-loss mechanism of the beam.

The correlation observed between measured beam-energy loss and that calculated from magnetic-field probe data indicates the importance of either direct measurements of induced electric fields (e.g., via Stark broadening measurements) or of magnetic-field profile measurements to establish an experimental link between postulated beam-loss mechanisms and observed propagation phenomena. Without this link, existing theoretical models could not be compared with the data measured in this study because assumptions relating to plasma conductivity and radial self-similarity were not well-fulfilled in the

experiments. Because significant net current density was observed out to a radius of 10 cm, it is clear that a drift tube of at least 20 cm in diameter would be required to establish experimental conditions where wall effects were negligible. Observed alterations of beam propagation at low pressures (270 Pa) resulting from the use of miniature magnetic-field probes indicate the desirability of nonintrusive field measurements, particularly at low pressures.

At the highest pressures used in this study (1600 Pa), observed conductivity levels indicated that avalanche ionization played a central role, whereas gas scattering was probably negligible. At pressures of $\sim 20\,000$ Pa, this situation could be reversed, providing experimental insight into this important parameter regime. Measured data suggest that beam rise-time is a crucial parameter in the conductivity generation. Also, it appears that the radial conductivity profile plays a central role in producing a stable pinch equilibrium. Therefore, further research is suggested on (1) high-pressure ($\geq 10\,000$ Pa) propagation, (2) the influence of guide tube walls, particularly on the net current profiles (3) beam conditioning (e.g., in a low-pressure tube) to vary the beam rise time, and (4) radially resolved measurements of beam and net current profiles. The suggested research could be performed for beams of modest energy where beam propagation distances are not great and could still provide useful fundamental data needed to resolve beam propagation issues of interest to the DARPA Chair Heritage program.

1.0 INTRODUCTION

The present experimental investigation was undertaken to provide information about electron-beam propagation under conditions which heretofore have not received experimental study. In particular, the pulse length for these experiments of 3 ns was approximately ten times shorter than generally used in other experiments.¹⁻⁷ Also, these experiments were performed in a 3.4 m diameter controlled-environment chamber, rather than in a drift tube, so that the nearest wall was sufficiently distant (~ 1 m) to preclude any possible effects on the beam propagation.

Specific objectives of this study included 1) measurements of beam-current temporal evolution and total energy transport for selected propagation distances, 2) measurements of the circumferential magnetic field as a function of time and radial distance, 3) open-shutter photography of beam propagation, 4) analyses of nose erosion rates, and 5) data analyses to determine operative mechanisms.

In the following report the experimental equipment and calibration procedures are discussed at the outset. Experimental results of beam and net current measurements and examples of features observed in the open-shutter photographs are then presented. Finally, model comparisons are discussed.

2.0 EQUIPMENT

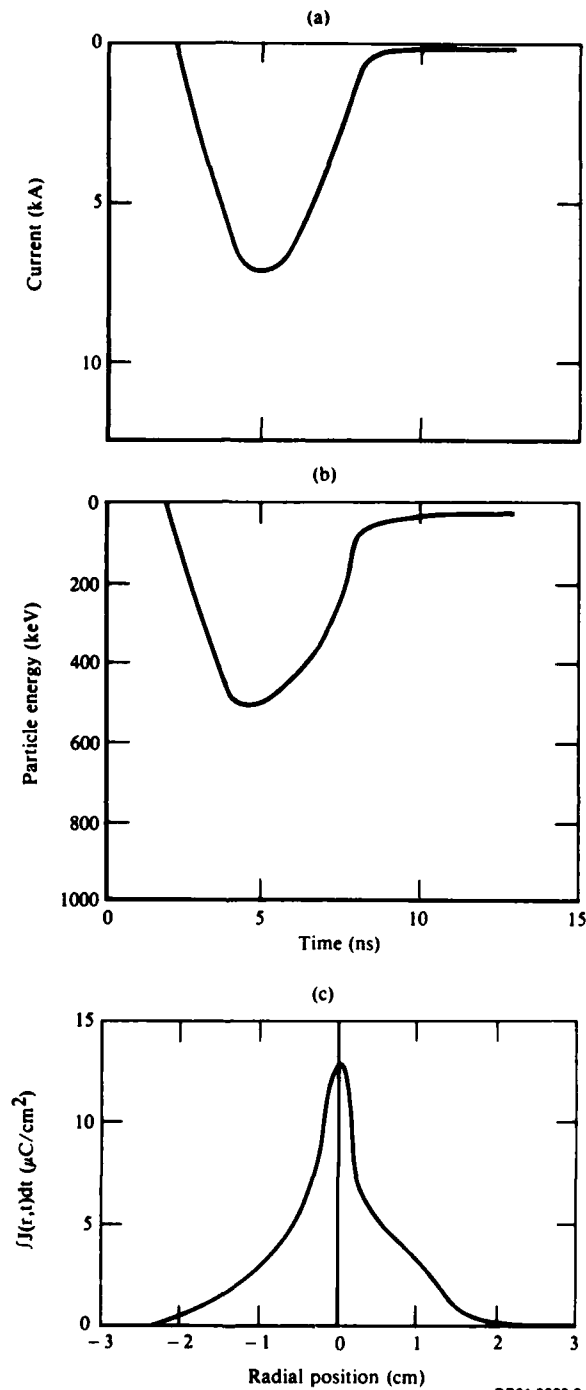
2.1 Beam Generator

The beam generator used for the MDRL experiments was the commercial Febetron 706.⁸ In this device, a Freon-insulated Marx generator charges an oil-insulated Blumlein-like structure in about 20 ns. A six-channel switch shorts the center conductor to the intermediate electrode of the Blumlein, producing the 3-ns output pulse. The output current, measured by a Faraday cup, described later, is shown in Figure 1a. The Febetron 706 does not have a diode voltage monitor. The diode voltage shown in Figure 1b was calculated by assuming a Child-Langmuir law dependence, i.e., $I_d = KV_d^{3/2}$, where I_d and V_d are diode current and voltage respectively and K is a constant depending on the diode geometry. K was found by setting $\int V_d I_d dt$ equal to the calorimetric measurement of total beam energy.

The time-integrated radial profile of beam current, Figure 1c, was found by using radiachromic film.³ This film consists of a transparent nylon sheet 50 μm thick, doped with a dye which becomes colored upon exposure to ionizing radiation. The film was enclosed in a 25 μm thick aluminum shield to prevent exposure by ultraviolet light or low-energy electrons. Quantitative measurement of the optical density produced by the beam was obtained using a Joyce-Loebel microdensitometer. Interference filters with a 10-nm bandwidth centered at 508.5 nm were used in front of the light source so that the densitometry was effectively at a single wavelength. Calibration curves of absorbed radiation dose as a function of optical density change were given by the film manufacturer.⁹

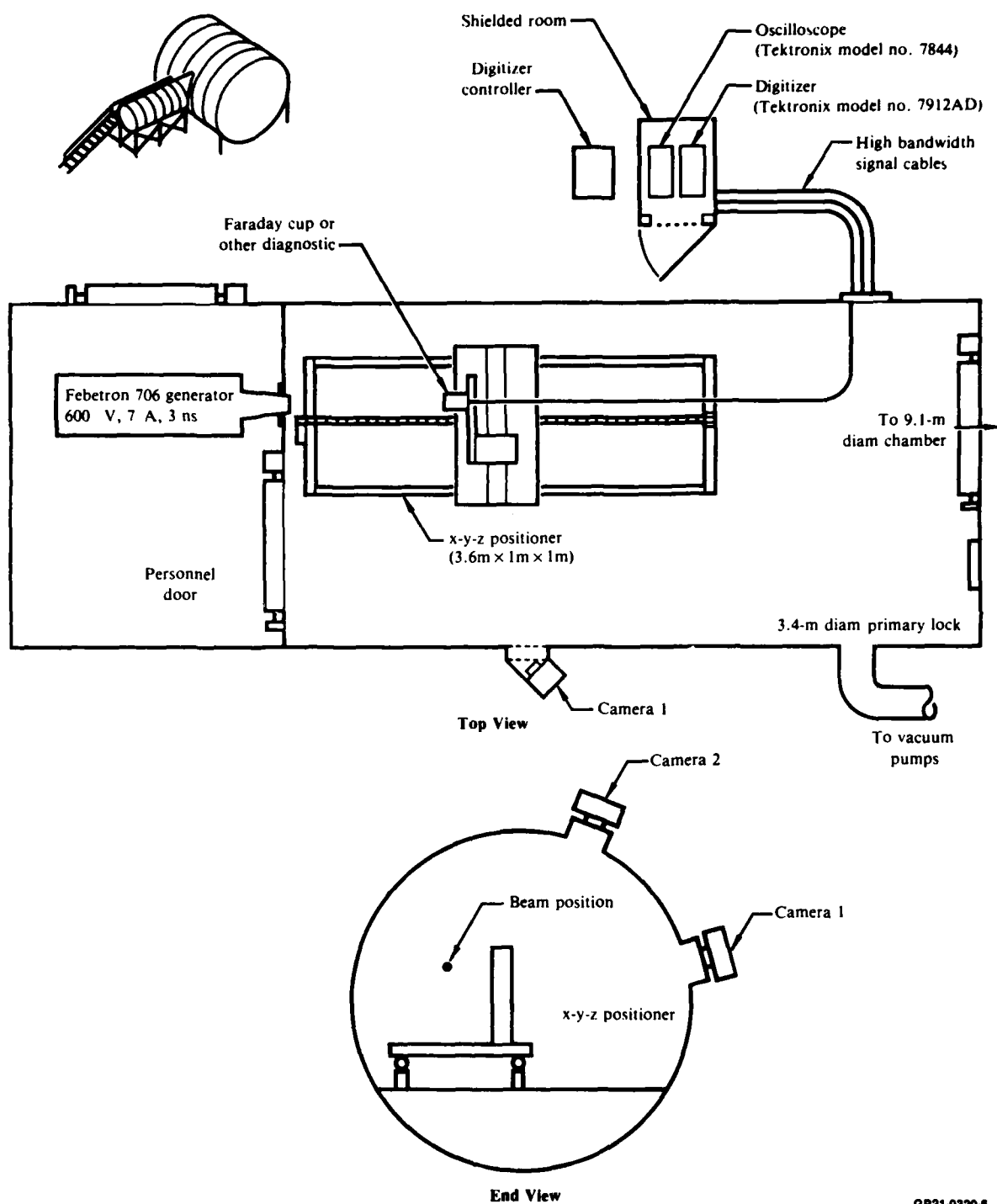
2.2 Controlled-Environment Chamber

For the present experiments, the Febetron 706 was coupled to the primary lock of a large (9.1 m diam) environmentally controlled chamber. This primary lock is 3.4 m in diameter and 6.1 m long. Because of the placement of the available entrance port, the beam was about 1 m from the nearest wall. Figure 2 shows top and end views of the location of the Febetron 706 and of the observation ports from which photographs were taken. The chamber was typically evacuated to 20 Pa (0.16 Torr) and then backfilled with synthetic air to operating pressure.



GP21-0320-2

Figure 1. (a) Febetron electron-beam current, measured with Faraday cup/calorimeter against anode foil, (b) Febetron electron-beam energy, calculated from (a) assuming Child-Langmuir-law voltage-current relationship, with $\int V I dt$ normalized to agree with calorimeter measurement, and (c) time-integrated radial profile of electron-beam current density based on radiachromic film data.



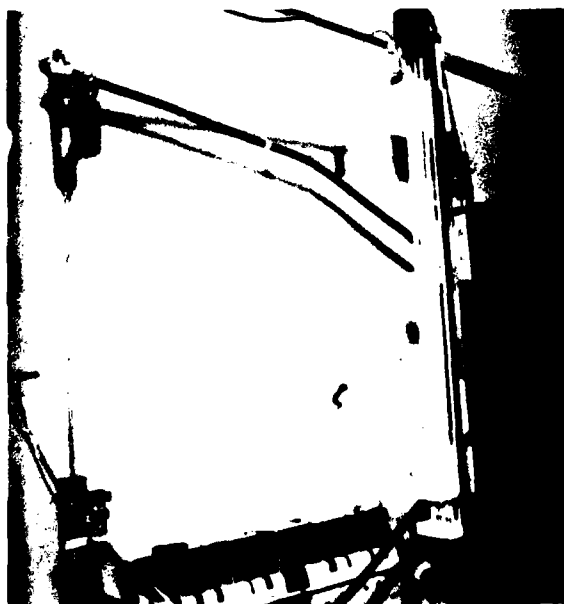
QP21-0320-8

Figure 2. Experimental arrangement for short-pulse electron-beam experiments in a 3.4-m diameter controlled-environment chamber.

2.3 Diagnostic Positioners

The xyz positioner (developed under an MDRL IRAD program), shown in Figure 2, permitted the remote positioning of diagnostics anywhere over a 3.6 m x 1 m x 1 m volume. A chain drive moved the carriage in the 3.6 m (z) direction, achieving a positioning accuracy of about 0.3 cm. Screw-drive mechanisms were used in the x and y directions, with an accuracy of 0.01 cm. Position was measured by rotation sensors coupled to the drive motors through magnetic clutches, needed to eliminate spurious signals from the rotation sensors caused by motor vibrations.

For magnetic-field-probe experiments, a special positioner was mounted on the xyz positioner which enabled the movement of two probes symmetrically in and out from the beam center in the radial direction. A single motor was geared to turn two screw-drives in opposite directions. A resistive slide wire provided positioning readout accurate to 0.1 cm. The probes were mounted on the screw-drives through long arms which were 35 cm away from the beam. Photographs showed that the probes could be held centered around the beam to within about 0.2 cm. A photograph of this positioner is shown in Figure 3.

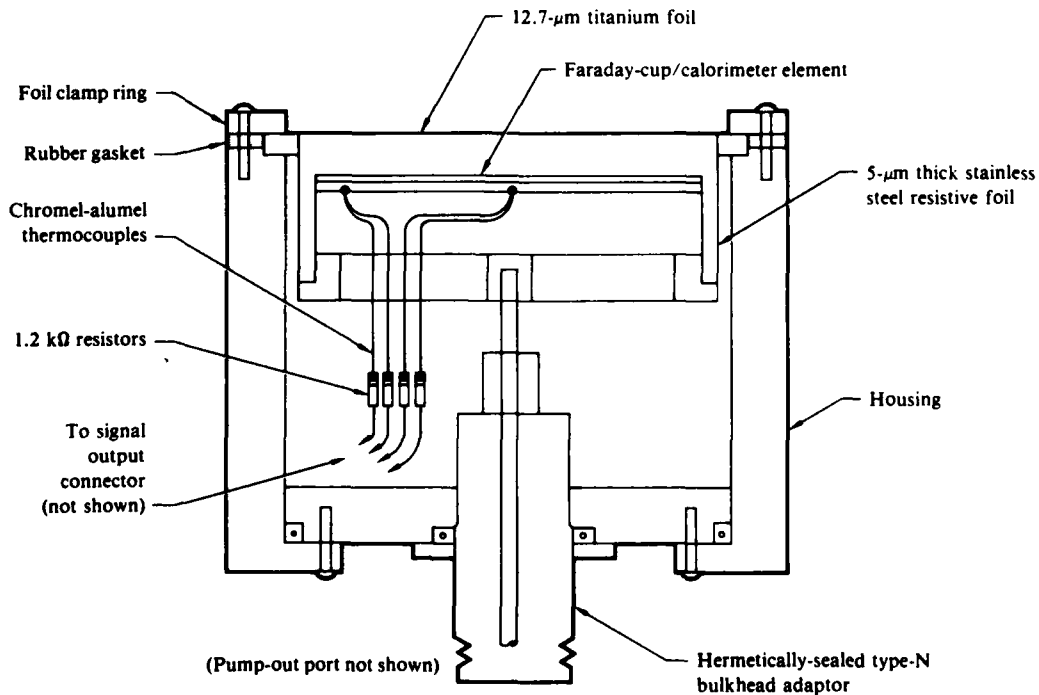


GP21-0320-13

Figure 3. Remotely controlled B_θ probe positioner installed in MDC controlled-environment chamber.

3.0 DIAGNOSTICS

A diagram of the Faraday cup/calorimeter is shown in Figure 4. A 12.7 μm Ti entrance foil absorbed plasma electrons (under 50 keV)¹⁰ and permitted a vacuum of $\lesssim 7$ Pa (0.05 Torr) to be maintained in the cup, at which pressure electron multiplication by the beam should be negligible. Solid-outer-conductor coaxial cable with a diameter of 1.3 cm and foam dielectric insulation was used to bring signals to the oscilloscope, preserving the rise-time of the signals and shielding unwanted noise. Calibration and rise-time of the Faraday cup were checked by discharging a coaxial line charged to a known voltage through a 50 Ω resistor into the collector of the cup. Calibration accuracy of $\pm 3\%$ or better is estimated. Figure 5 shows the calibration arrangement and a typical calibration trace. The combined rise time of the system is ~ 1.3 ns.



GP21-0320-5

Figure 4. Faraday-cup/calorimeter used in short-pulse relativistic electron-beam experiments.

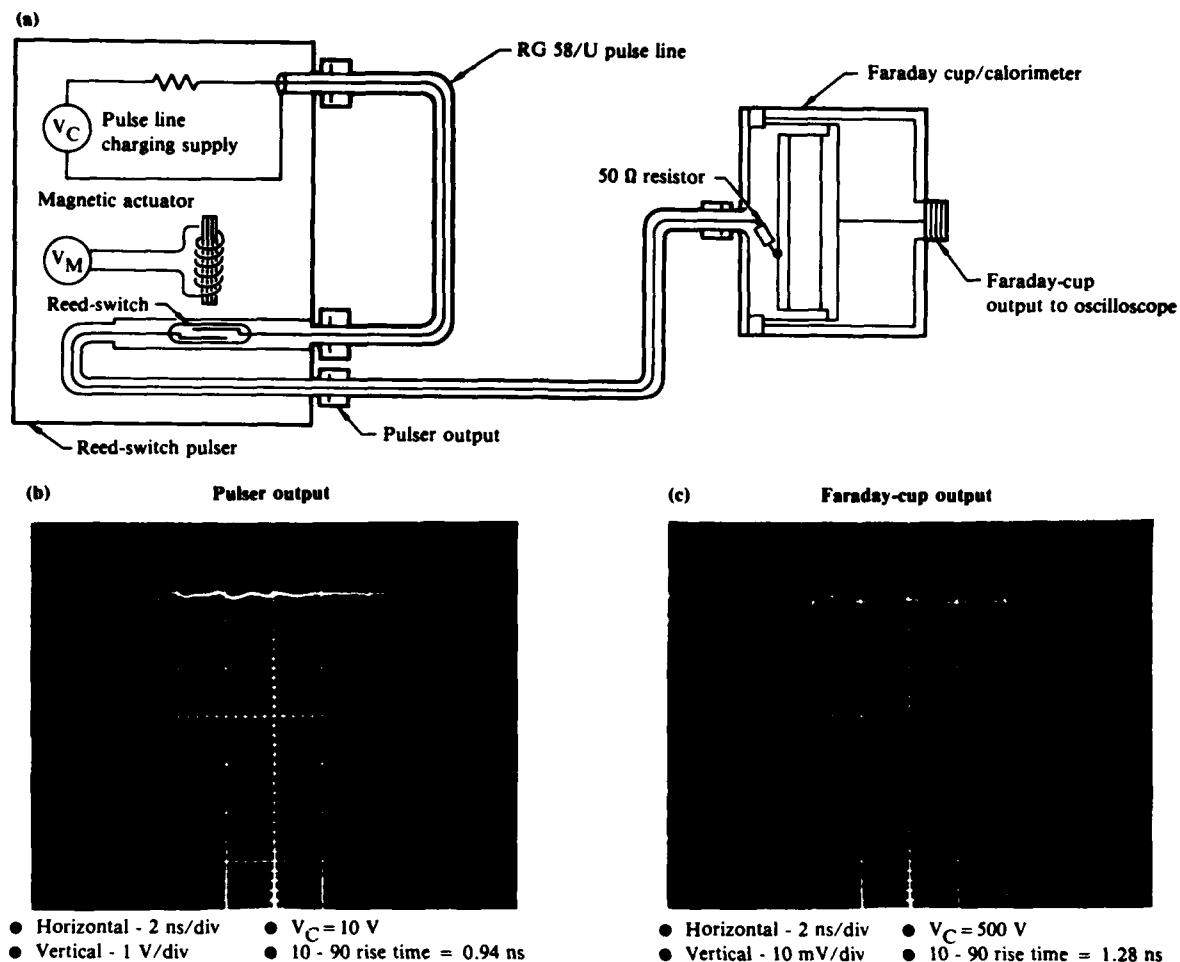
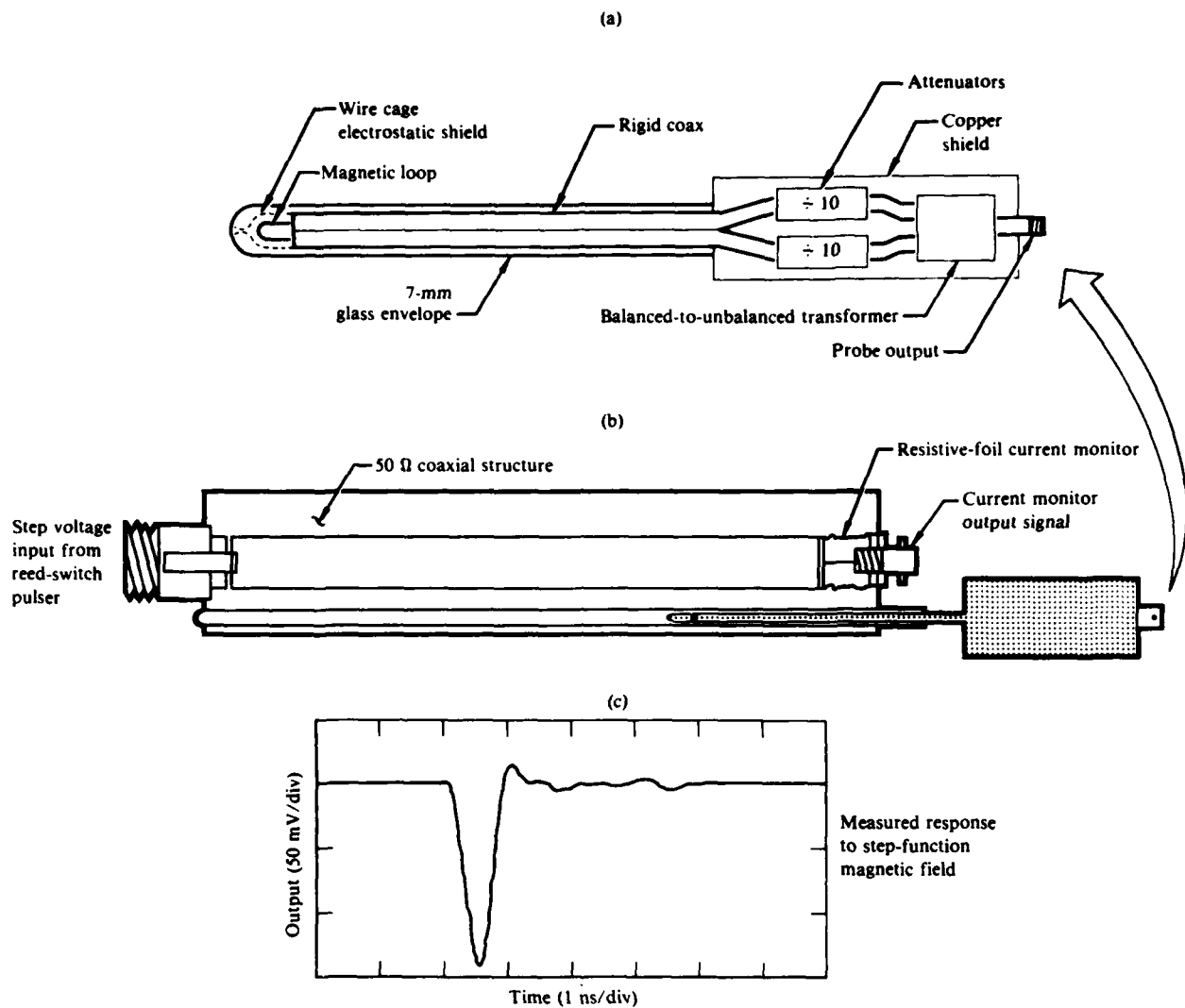


Figure 5. (a) Reed-switch pulser arrangement for calibration of Faraday cup, (b) pulser output, and (c) Faraday-cup output.

GP21-0320-7

A diagram of the magnetic field probes, their calibration set-up, and a typical calibration output is shown in Figure 6. The balanced magnetic loop was constructed by removing 1.75 cm from the outer jacket of rigid 0.22 cm diameter coax at the midpoint of a 50 cm length, and then folding it in half about this point. Thus the center conductor and insulating dielectric are continuous, preventing breakdown from the large dB/dt -induced loop voltages (≥ 300 V under certain conditions). The probe is shielded by a wire cage consisting of ~ 80 enameled #36 wires (0.014 cm diameter), soldered at one end to the outer conductor of the rigid coax, but insulated from each other at the other end. This cage presents a nearly solid conducting shield to an electric field, but it presents little perturbation to a magnetic field line. The sig-



QP21-0320-9

Figure 6. Diagram of a magnetic-field probe used in electron-beam experiments, (b) calibration arrangement for applying an accurately-known step magnetic field to the probe, and (c) typical probe output recorded with a sampling scope having a bandwidth >1 GHz.

nals from the two ends of the rigid coax were passed through 1/10 attenuators with 1 GHz bandwidth (Tektronix 011-0059-02), a balanced-to-unbalanced transformer (Minicircuits Corp. ZFSCJ-2-1, with modified connector placement) and brought to the oscilloscopes by 1.3 cm diam Heliax cable. Calibration accuracy to $\sim 3\%$ was achieved by numerical integration of the step response of the probes and comparison of the result with the current monitor signal.

3.1 Signal Acquisition

A dual-beam oscilloscope (Tektronix 7844) with a P-11 phosphor and film fogger to give rapid photographic writing speed was used for Faraday cup and magnetic probe signal acquisition. In addition, a transient digitizer (Tektronix 7912AD), controlled by a microcomputer (Digital Equipment Corp. MINC-11) was used for magnetic probe signal acquisition. The scope-digitizer combination permitted a second probe signal to be recorded on the oscilloscope along with the Febetron monitor signal to obtain timing information.

3.2 Experimental Results

The first experimental question addressed was the degree of rectilinear beam propagation in the controlled-environment chamber. Previous experiments in a 7.6 cm diameter glass guide tube showed that the Febetron beam would follow a 10^0 bend in the tube with little loss (Figure 7). This result indicated that rectilinear propagation in a straight tube might be due to the tube walls. Open chamber experiments, however, did not show a requirement for guiding wall effects for rectilinear propagation. Variation in the transverse beam position at a propagation distance of 180 cm in the chamber was reliably $\lesssim 1$ cm. At 120 cm distance, it was usually < 2 mm, the estimate being limited by the resolution of the photographs. The beam position was apparently unaffected by the position of the Faraday cup or the magnetic probes. Figure 8 shows an example of this immunity from the proximity of conducting bodies. Note that the beam position did not move measurably when the Faraday cup was moved off center.

To center the beam, it was necessary to use two cameras viewing the beam from different angles to measure the beam position with respect to the x and y axes. Figure 9 shows views from each camera of a typical shot with magnetic probes at $z = 120$ cm, after the probes have been carefully centered. For purposes of scaling, note that the diameter of the probe jacket is 7 mm.

Faraday-cup/calorimeter measurements were performed at propagation distances of $z = 5.7, 10, 15, 30, 60, 120,$ and 180 cm at pressures of 75-1600 Pa (0.5 Torr - 12 Torr). Behavior is generally similar to that observed in an insulating 7.6 cm diam guide tube, with a low-pressure window for propagation at 270-800 Pa (2-6 Torr), and poor propagation at lower and higher pressures.

P = 400 Pa (3 Torr)
22.5° bend, f/5.6 aperture



P = 400 Pa (3 Torr)
10° bend, f/11 aperture



P = 1070 Pa (8 Torr)
10° bend, f/5.6 aperture



GP21-0320-15

Figure 7. Typical open-shutter photographs of propagation in bent guide tubes.

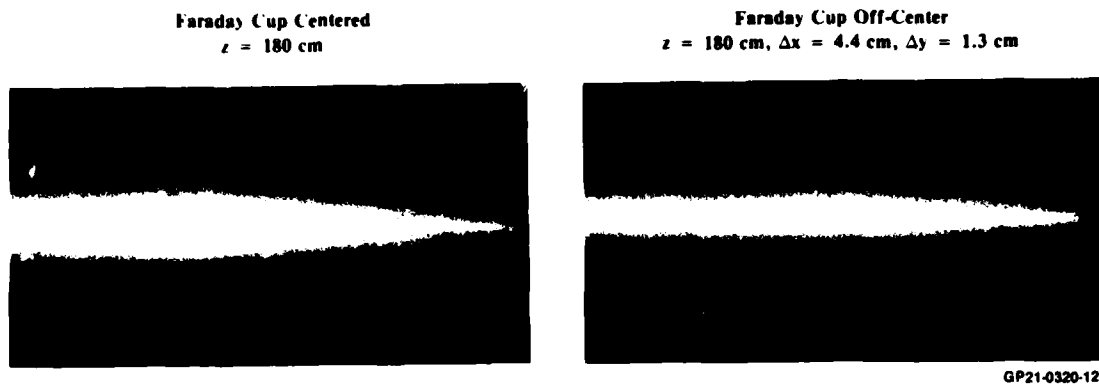


Figure 8. Open-shutter photographs of a Febetron 706 electron beam propagating in a controlled-environment chamber at 530 Pa (4 Torr) showing that the beam position is not affected by movement of the Faraday cup.

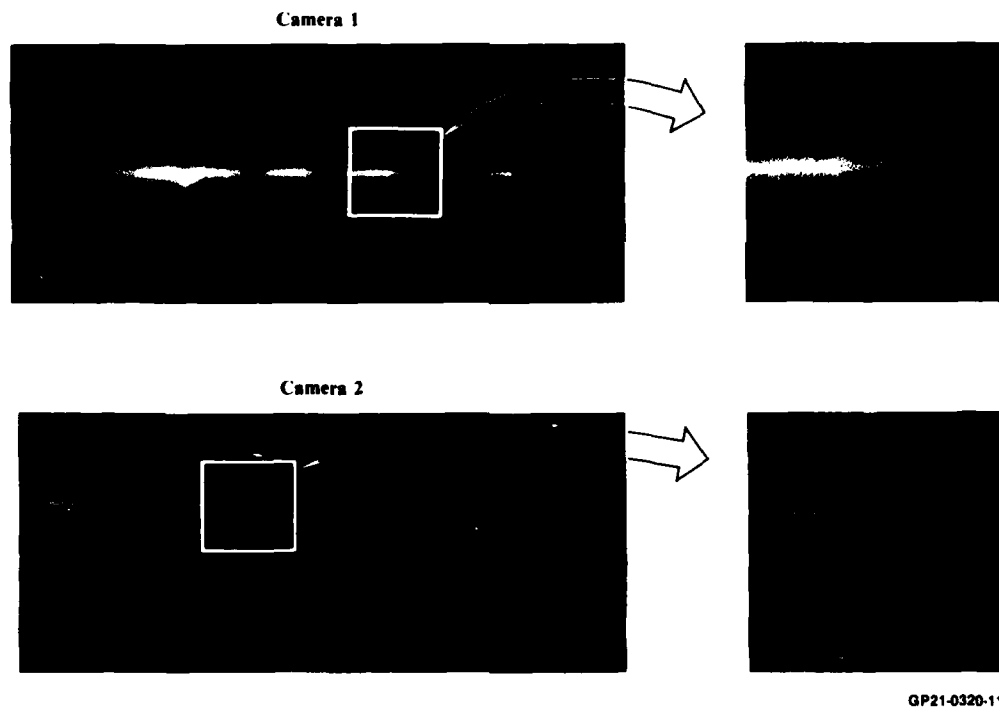
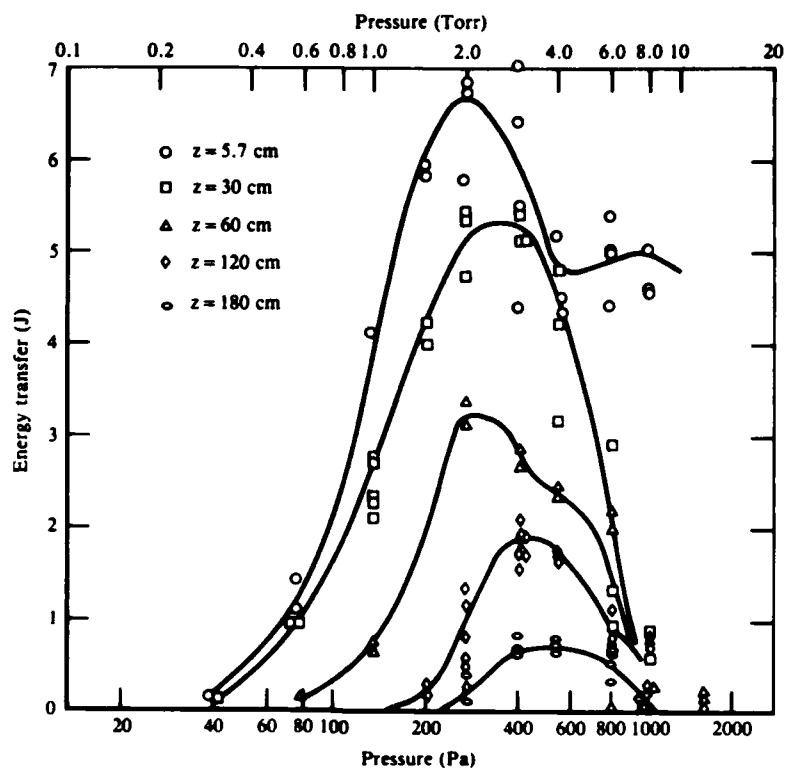


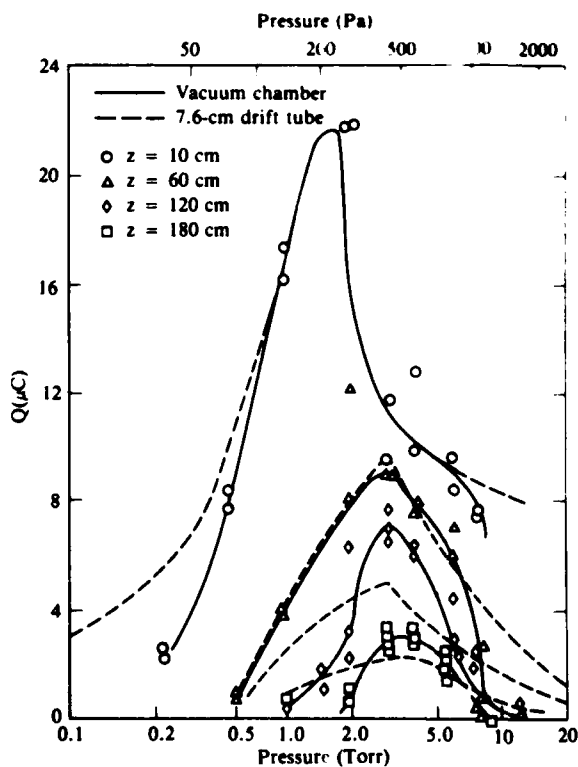
Figure 9. \dot{B}_θ probes at $z = 120 \text{ cm}$, pressure = 530 Pa (4 Torr).

Figures 10 and 11 show data giving total energy and total beam charge transfer as a function of pressure with propagation distance z as a parameter. In Figure 11, drift tube data are shown for comparison. The primary difference is that the window is narrower, but with better propagation at the optimal pressure of 3-4 Torr.



GP21-0320-3

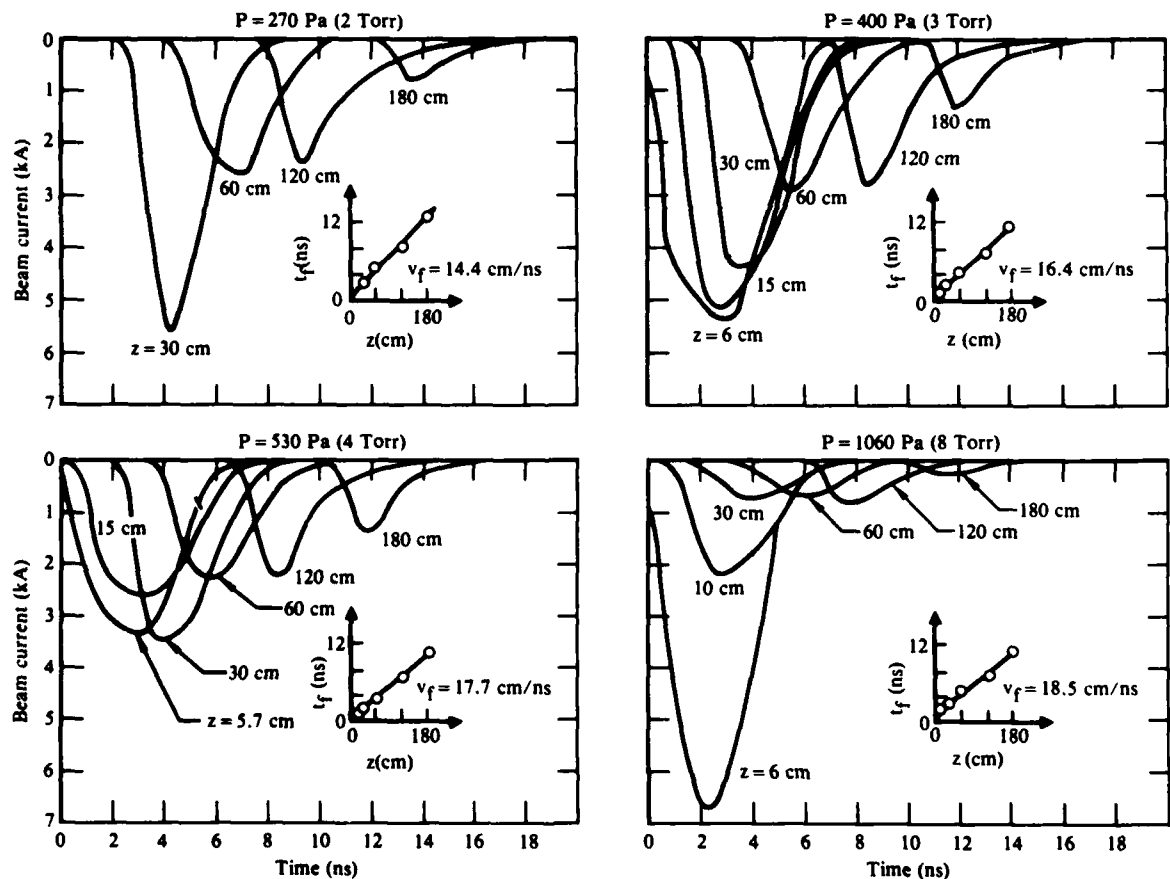
Figure 10. Energy transfer measured by calorimeter in a controlled-environment chamber.



GP21-0320-14

Figure 11. Total charge collected by Faraday cup as a function of pressure in a controlled-environment chamber (solid curves) with drift-tube data (dashed curves) shown for comparison. All symbols apply to chamber data; drift-tube data points are not shown.

The beam front velocity was determined by using a dual-beam oscilloscope with Faraday cup signals on one beam and the Febetron Blumlein monitor on the other beam. The sharp break in the monitor signal when the Blumlein switch fired provided a timing reference point accurate to $\sim \pm 0.25$ ns. Figure 12 shows a series of Faraday cup traces showing the progress of the pulse in time at pressures of 270-1070 Pa. Table 1 gives front velocity data and computed nose-erosion velocity, based on $\langle v_z \rangle$ of the electrons of $\beta c (1 + I_{\text{net}}/I_{\text{Alfven}})^{-1/2}$, calculated for a pinched-beam equilibrium.¹¹ For the average injection energy of 400 keV and $I_{\text{net}} \approx 2$ kA, this gives $\langle v_z \rangle = 24$ cm/ns, with about ± 1 cm/ns accuracy estimated. Beam-front velocity values measured in an insulating drift tube are also given in Table 1. Within experimental error, the beam-front velocity results are the same in the drift tube as in the large chamber.



GP21-0320-4

Figure 12. Time-correlated Faraday-cup traces showing beam-front velocity. The front arrival was taken at the time the beam current reached 500 A. A plot of the front arrival time, t_f , as a function of z is shown in the insets. v_f is the beam-front velocity determined from the plots.

TABLE 1. BEAM FRONT-VELOCITY DATA.

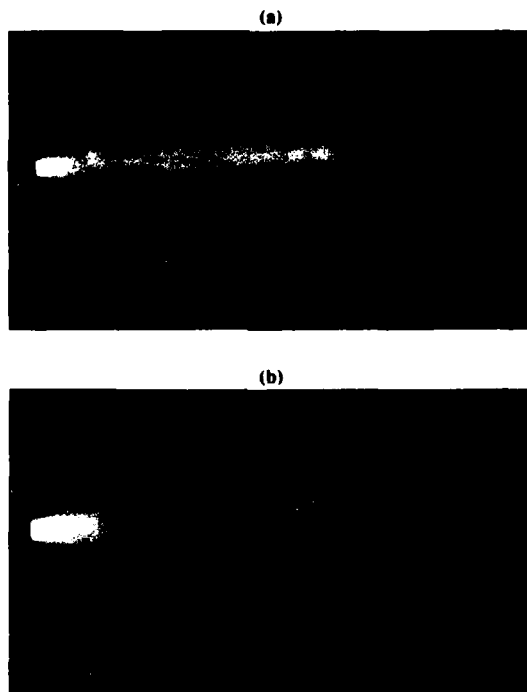
Pressure [Pa (Torr)]	7.6-cm diam glass tube (cm/ns)	7.6-cm diam glass tube w/conducting screen outside (cm/ns)	3.4-m diam space chamber (cm/ns)
75 (1.0)	14.3	13.3	—
130 (2.0)	15.4	13.0	14.4
270 (3.0)	15.8	15.6	16.4
540 (4.0)	17.6	16.7	17.7
1070 (8.0)	18.2	17.3	18.5

- Nose erosion velocity $\equiv v_{ne} = \langle v_z \rangle - v_{front}$
 $\cong 24 \text{ nm/ns} - v_{front}$

GP21-0320-1

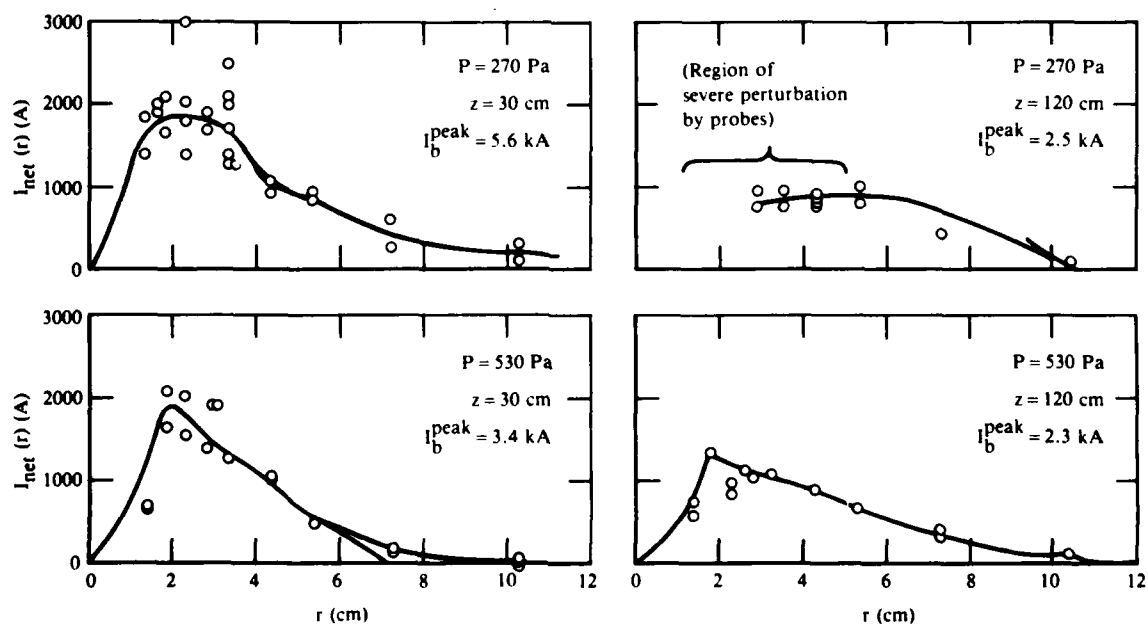
At high pressures ($> 530 \text{ Pa}$), the loss of the beam tail appears to be important, as was the case in an insulating drift tube. This effect is shown by the time-correlated Faraday-cup signals shown in Figure 12. At 400 Pa (3 Torr), the difference in arrival times of the trailing edge of the beam between $z = 6 \text{ cm}$ and $z = 120 \text{ cm}$ is about 4.5 ns , which is consistent with the estimate given above for $\langle v_z \rangle$ of the electrons. At 1070 Pa (8 Torr), the time difference is about 3 ns , showing that some of the beam tail is lost before reaching $z = 120 \text{ cm}$. The effect appears to be more pronounced in the space chamber than in the drift tube, and more erratic, which explains the large scatter in data and narrow pressure window seen in Figure 10. Open-shutter photographs also show this scatter as evidenced by Figure 13 which shows two shots at 1070 Pa with injection parameters apparently identical. Note the complete lack of a beam pinch in Figure 13b. Apparently the guide tube wall (or possibly a plasma formed on the walls) exerts a stabilizing influence on the beam tail.

Magnetic-field probes were used to measure the radial magnetic field structure and to gain some understanding of the charge return mechanism. Figure 14 shows net current $I_{net}(r)$ contained within a circle of radius r as a function of r at pressures of 270 and 530 Pa (2 and 4 Torr). Data shown are at 2 ns from beam front arrival. The observed temporal behavior was similar at all positions. At 270 Pa , the B-fields rose to $\sim 75\%$ of their maximum level in 2 ns , gradually increased for $2\text{--}3 \text{ ns}$ more, and then remained reasonably constant for the remainder of the observation time of $\sim 20 \text{ ns}$. (Because



GP21-0320-17

Figure 13. Open-shutter photographs at 1070 Pa (8 Torr) showing large shot-to-shot variations.



GP21-0320-8

Figure 14. Magnetic-probe data (net current) as a function of radial position. Peak beam current, I_{peak} , averaged over three shots at each position is also shown. Data are at 2 ns after the beam-front arrival.

\dot{B} was so small during the decay of the fields after the beam, a quantitative measurement of this decay was not possible because of the inadequate signal-to-noise ratio). At 530 Pa, the net current reached its peak in ~ 1 -2 ns; in many cases, the rise-time of the \dot{B} signals was limited by the 500 MHz bandwidth of the signal acquisition system. Both the 270 and 530 Pa magnetic-field data indicate that a significant return current flows out to a radius of ~ 10.3 cm.

The question of probe perturbation of the current flow was addressed experimentally only by observation with open-shutter photographs. It was observed (Figure 15) that at $z = 120$ cm and a pressure of 270 Pa (2 Torr), the probe perturbation was severe even with the probes well outside the beam and intercepting a small percentage of the area of the current channel. The mechanism of this perturbation is unclear. It is true that probes can cool an area around them causing a "hole" in the conducting plasma which is larger than the physical size of the probe. However, over such a short time scale, the perturbation by the probe could travel a distance on the order of the electron thermal velocity times the time scale of interest, which is only a few millimeters.

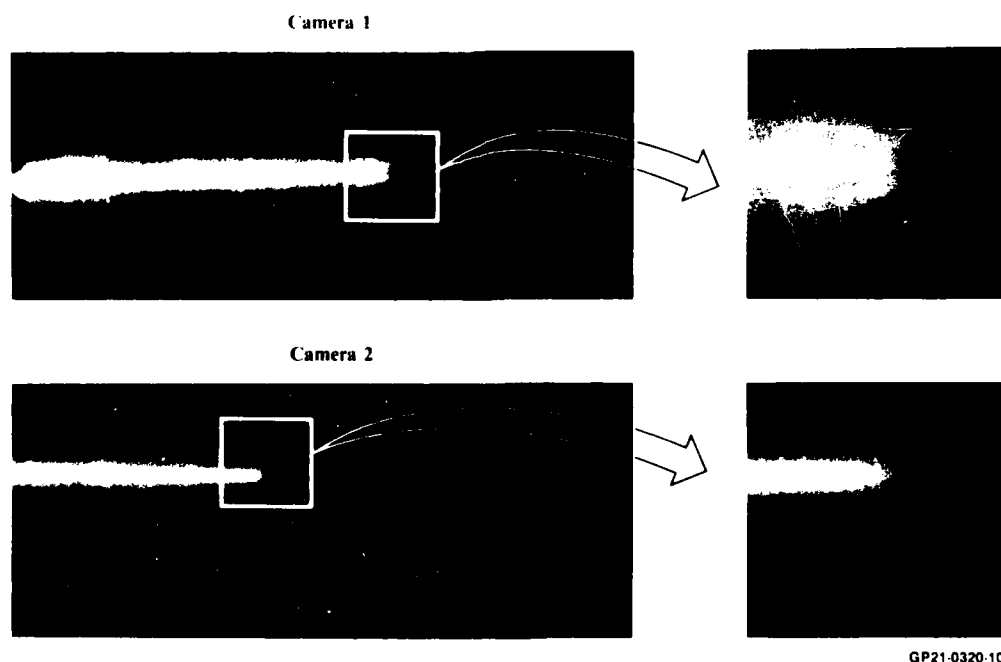


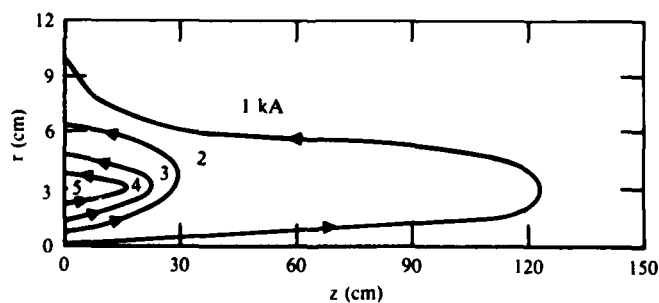
Figure 15. Open-shutter photographs of beam propagation at $P = 270$ Pa showing severe perturbation caused by the magnetic-field probes. The probes are located at a propagation distance of $z = 120$ cm and at a radius of $r = 4.3$ cm (the end of the glass probe-envelope is at $r = 2.9$ cm).

A more likely explanation for the observed disrupting effects of the probes is as follows. In order to form a pinched beam equilibrium and still have adequate charge return for the beam to propagate, the plasma halo surrounding the beam is crucial. The formation of this plasma halo probably occurs primarily from ionization by the expanded beam nose and avalanche multiplication in the strong radial electric fields. If the probes short the electric fields around them, the formation of the halo could be disrupted, causing poor pinch formation.

The fractional current neutralization in the beam channel, as given by one minus measured peak net current divided by peak beam current, is in the range 40-60%. The actual peak net current is probably somewhat greater and thus the neutralization somewhat less, because when the probes are close to the edge of the beam channel, the glass shields intercept about 25% of the beam.

The net current measurements indicate that little net charge is propagated. A qualitative topological diagram of net current flow is shown in Figure 16. Each of the contours in Figure 16 depicts the radii beyond which 1 kA of set current flows out and returns. Plasma conductivity continues long after the beam is over, with the pattern of Figure 16 persisting for tens of nanoseconds. A crude circuit model of this configuration as an inductance L in series with a resistance R suggests a decay time of $L/R = \mu_0 \sigma r_b^2/2$, where σ is the conductivity and r_b the beam radius.

At times of 4-6 ns after the beam arrival, large \dot{B} signals are seen at radii from 4-10 cm, which are not symmetrical about the beam but are moder-



GP21-0320-16

Figure 16. Topology of net current flow. Each line represents the boundary of a flux tube inside of which ~1 kA of net current flows.

ately reproducible on a shot-to-shot basis. At radii of 3.3 cm and less, these large asymmetrical \dot{B} signals never occur; they occur occasionally at 4.3 cm, and almost always at larger radii, though with variation in amplitude. The observed fluctuations may indicate instability of the beam tail, perhaps caused by the probe.

4.0 MODEL COMPARISON

Electron-beam nose models show erosion caused by the beam energy loss in the inductive fields at the beam nose^{12,13} and the beam electrons scattering off the neutral gas background.^{14,15} In the absence of these effects, Briggs has argued that erosion rates should approach zero asymptotically with propagation distance on a scale length of a few beam radii,¹⁴ at least for highly relativistic beams where $1/\gamma^2 \ll 1$. Because the MDRL experiments have been performed at low pressures where gas scattering effects are probably unimportant, the following analysis concentrates on the inductive energy loss mechanism.

Sharp and Lampe¹³ give the simple expression

$$v_{ne}/c = \left(1 + \frac{mc^3}{e} \frac{\gamma - 1}{\lambda_{\infty} I_b}\right) \quad (1)$$

for nose erosion velocity v_{ne} caused by the beam energy loss in the inductive electric field. In Equation (1), λ_{∞} is $\ln(r_c^2/r_b^2)$, where r_b is the beam radius and r_c is the radius of the conducting channel. This formula agrees well with a more elaborate calculation which assumes $\gamma \gg 1$, self-similar beam expansion in the radial direction, and conductivity generation without avalanche processes.

Because of the foregoing assumptions, a direct comparison of this formula with the MDRL measured data is of little value. However, it is possible to estimate beam energy loss resulting from the induced electric fields using measured magnetic probe data. The procedure is to compute the induced electric field E_z from the probe data, compute the energy loss rate of the beam, and compare these values with the measured energy loss rate.

Using Faraday's law, $\nabla \times E = \partial B/\partial t$ and neglecting $\partial E_r/\partial z$, E_z can be estimated as

$$E_z(r, t) = \int_r^c \dot{B}_{\theta}(r', t) dr' , \quad (2)$$

where r_c is the channel radius, taken as 10.3 cm, outside of which \dot{B}_θ is very small. Thus the energy deposited by the beam electrons per unit length per unit time is given by

$$\frac{\partial^2 W}{\partial z \partial t} = 2\pi \int_0^{r_b} dr r J_b(r, t) \int_r^{r_c} \dot{B}_\theta(r', t) dr' . \quad (3)$$

Equation (3) can be evaluated to a reasonable approximation by taking the lower limit of the inner integral as $r_b/2$, so that the inner integral is a constant independent of r .

$J_b(r, t)$ can then be integrated over the beam area, giving

$$\frac{\partial^2 W}{\partial z \partial t} \approx I_b(t) \int_{r_b/2}^{r_c} \dot{B}_\theta(r', t) dr' . \quad (4)$$

Integration of Equation (4) in time gives beam energy deposition per unit length:

$$\frac{\partial W}{\partial z} \approx \int dt I(t) \int_{r_b/2}^{r_c} \dot{B}_\theta(r, t) dr . \quad (5)$$

Typically, the \dot{B}_θ signals are a spike of ~ 2 ns duration at the beginning of the beam pulse, confirming that most of this energy is taken from the nose of the beam.

The most straightforward comparison of this model with experimental data is with calorimetric data as plotted in Figure 17 to illustrate energy loss rate. The average energy loss at 530 Pa between 5.7 and 60 cm is 3.3 J/m. Using Faraday cup and magnetic probe data, numerical integration of Equation (5) at a pressure of 530 Pa and $z = 30$ cm gives a value of ~ 2.5 J/m. A fairly large uncertainty exists in this figure (perhaps $\sim \pm 30\%$) because of scatter in the data, possible probe perturbation of the current channel, degradation of the signal rise time, and a lack of precise time correlation

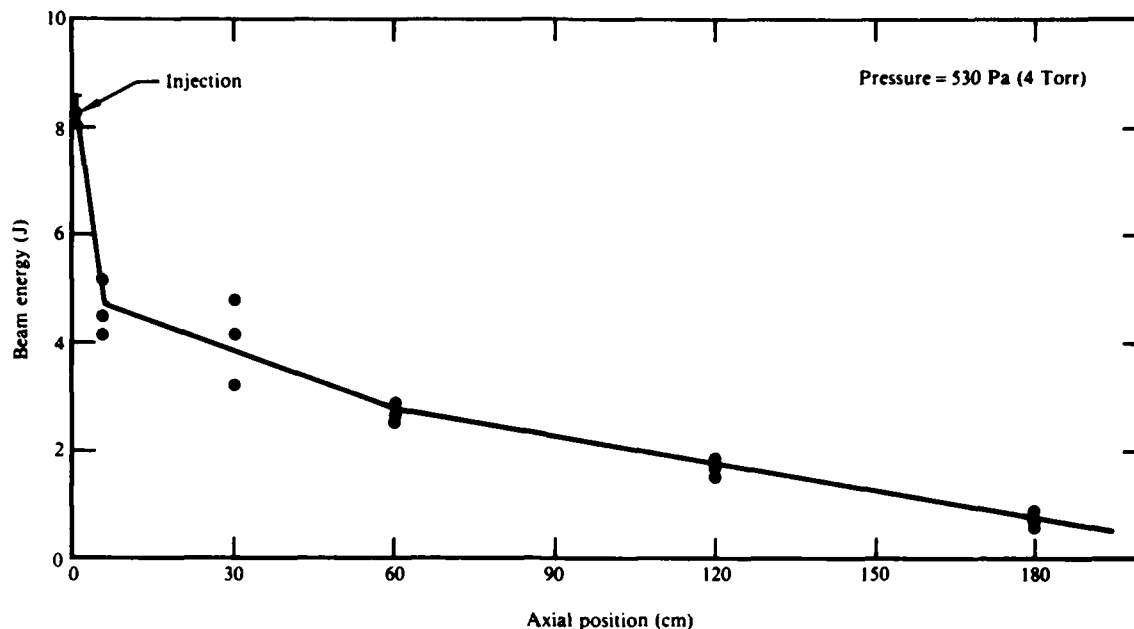


Figure 17. Calorimeter data at a pressure of 530 Pa, plotted as a function of axial position (z) to show beam energy loss per unit length.

between Faraday cup and magnetic probe signals resulting from an unfortunate equipment failure (beam two of the dual-beam oscilloscope failed). Nevertheless, the result is an indication that the inductive energy loss mechanism at the beam nose is the primary limit to the beam propagation at 530 Pa (4 Torr). At the same pressure and $z = 120$ cm, a value of 1.2 J/m is obtained from Equation (5). Measured calorimeter data at this pressure show an average energy loss of 1.8 J/m between 60 and 180 cm, which is in reasonable accord with the predicted value.

Comparisons of this simple model with data at other pressures were not made. At 1070 Pa (8 Torr), the shot-to-shot variation precluded any meaningful radial B_θ profile measurements. At 270 Pa (2 Torr), the photographs show that the probes perturb the beam propagation severely (Figure 15). Nevertheless, some qualitative observations can be made. Front velocities decrease substantially with decreasing pressure between 75 Pa and 530 Pa, in the same manner as in an insulating drift tube. Magnetic probe data at 270 Pa (2 Torr) in the drift tube (where the beam was not so severely perturbed) showed larger B_θ signals than at 530 Pa (4 Torr) which correlate well with the faster nose erosion rate observed.

5.0 CONCLUSIONS

Propagation of a 500 keV, 7kA, 3 ns electron beam has been studied in a 3.4 m diameter controlled environment chamber at air pressures from 75-1600 Pa (0.56-12 Torr). A Faraday cup, magnetic-field probes, and open-shutter photography were the principal diagnostics used. Optimal propagation was observed at 3-4 Torr. At lower pressures, rapid nose erosion reduced the propagation efficiency, whereas at higher pressures, the beam suffered a lack of a stable reproducible pinch equilibrium, causing the beam to freely expand. Reasonable agreement was obtained between observed nose erosion of the beam and a model based on erosion caused by the induced axial electric fields at the beam nose. In the model, the induced fields were deduced from \dot{B}_θ probe measurements, rather than calculated from first principles.

References

1. M. L. Andrews, H. Davitian, D. A. Hammer, H. H. Fleischman, J. A. Nation, and N. Rostoker, On the Propagation of High-Current Beams of Relativistic Electrons in Gases, *Appl. Phys. Letters* 16, 98 (1970).
2. M. L. Andrews, H. Davitian, H. H. Fleischmann, and J. A. Nation, Ionization Instability in the Propagation of High-Current Relativistic Electron Beams in Gases, *Phys. Fluids* 14, 2553 (1971).
3. S. F. Greybill, Dynamics of Pulsed High Current Relativistic Electron Beams, *IEEE Trans. Nucl. Sci.* NS-18, 438 (1971).
4. P. A. Miller, J. B. Gerardo, and J. W. Poukey, Relativistic Electron Beam Propagation in Low-Pressure Gases, *J. Appl. Phys.* 43, 3001 (1972).
5. P. A. Miller and J. B. Gerardo, Relativistic Electron Beam Propagation in High-Pressure Gases, *J. Appl. Phys.* 43, 3008 (1972).
6. B. Ecker and S. Putnam, Collective Ion Acceleration and Power Balance in Intense Electron Beams in Neutral Gas, *IEEE Trans. Nucl. Sci.* NS-24, 1665 (1977).
7. T. J. Fessenden, R. J. Briggs, J. C. Clark, E. J. Lauer, and D. O. Trimble, FX-25 Beam Propagation Experiments, Lawrence Livermore Laboratory Report No. UCD-17840 (20 June 1978).
8. Presently manufactured by Hewlett-Packard Corp., McMinnville, OR.
9. Radiachromic-Note 4 (Far West Technology, Inc., Goleta, CA).
10. L. Pages, E. Bertel, H. Jaffe, and L. Sklavenitis, Energy Loss, Range and Bremsstrahlung Yield for 10 keV to 100 MeV Electrons, *Atomic Data* 4, 31 (1972).
11. 1980 McDonnell Douglas Independent Research and Development Report, MDC Q0857-4, Vol. 1, p. 104012.13, 14 Jan 1980.
12. E. P. Lee and D. M. Cox, Beam Head Erosion, Lawrence Livermore Laboratory Report No. UCID 17929 (13 September 1978).
13. W. M. Sharp and M. Lampe, Steady-State Treatment of Relativistic Electron Beam Erosion, *Phys. Fluids* 23, 2383 (1980).

14. R. J. Briggs, Estimates of Nose Erosion Rates Due to Gas Scattering Plus the Charge Neutralization Dynamics, Lawrence Livermore Laboratory, Informal memo MFE/BR/80-56 (March 1980).
15. F. W. Chambers and J. A. Masamitsu, Beam Erosion Rates - Comparison of Analytic and Computed Results, Lawrence Livermore Laboratory Report No. UCID 18746 (1980).

DISTRIBUTION

	Copies		Copies
Defense Advanced Research Projects Agency		U.S. Army Ballistic Research Laboratory	
ATTN: J. Mangano	1	ATTN: Dr. D. Eccleshall	1
Maj. R. Gullickson	1	DRDAR-BLB	
1400 Wilson Boulevard		Aberdeen Proving Ground, MD	
Arlington, VA 22209		21005	
Department of the Navy		Ballistic Missile Defence	
Navy Material Command		Advanced Technology Center	
ATTN: Dr. D. Finkleman	1	ATTN: Mr. M. Hawie	1
MAT-08T-2		BMDSATC-1	
Washington, DC 20362		P.O. Box 1500	
		Huntsville, AL 35807	
Department of the Navy		Commander, Harry Diamond	
Chief of Naval Operations		Laboratories	
ATTN: Dr. C. F. Sharn	1	ATTN: S. Graybill	1
OP 987		Branch 22300	
Washington, DC 20350		2800 Powder Mill Road	
Commander, Navel Research Laboratory		Adelphi, MD 20783	
ATTN: Dr. J. Aviles	1	Central Intelligence Agency	
Dr. M. Lampe	1	ATTN: Dr. C. Miller/OSI	1
Dr. R. Greig	1	P.O. Box 1925	
Washington, DC 20375		Washington, DC 20013	
Office of Naval Research		Defense Technical Information	
ATTN: Dr. T. Berlincourt	1	Center	
Dr. W. Condell	1	Cameron Station	1
Code 410		Alexandria, VA 22314	
Arlington, VA 20360		Department of Energy	
Office of Naval Technology		ATTN: Dr. J. Leiss, G-256	1
ATTN: Dr. Eli Zimet	1	Mr. G. Peters, G-256	1
MAT-0727		Dr. T. Godlove, MC-404	1
800 North Quincy Street		Washington, DC 20545	
Arlington, VA 22217		Commander, Foreign Technology	
Naval Postgraduate School		Division	
ATTN: Prof. K. Woehler	1	ATTN: J. S. Williams/ETET	1
Dept. of Physics		Wright-Patterson Air Force	
Monterey, CA 93940		Base, OH 45433	
Air Force Weapons Laboratory		AVCO-Everett Research Laboratory,	
Kirtland Air Force Base		Inc.	
ATTN: Dr. D. Straw	1	ATTN: Dr. R. Patrick	1
Albuquerque, NM 87117		2385 Revere Beach Parkway	
		Everett, MA 02149	

	Copies		Copies
B-K Dynamics, Inc. ATTN: Dr. R. Linz 3204 Monroe Street Box 6012 Rockville, MD 20850	1	Physics International ATTN: Dr. S. Putnam 2700 Merced Street San Leandro, CA 94577	1
The Charles Stark Draper Laboratory, Inc. ATTN: Mr. E. Olsson 555 Technology Square Cambridge, MA 02139	1	Physical Dynamics, Inc. ATTN: Dr. K. Brueckner P.O. Box 556 La Jolla, CA 92037	1
IRT Corporation ATTN: Mr. W. Selph P.O. Box 80817 San Diego, CA 92138	1	The Rand Corporation ATTN: Dr. S. Kassel 2100 M Street, N.W. Washington, DC 20037	1
JAYCOR ATTN: Dr. D. Tidman 205 South Whiting Street Alexandria, VA 22304	1	Sandia Laboratories ATTN: Mail Services Section for Dr. R. B. Miller Albuquerque, NM 87115	1
Lawrence Livermore National Laboratory ATTN: Dr. R. Briggs Dr. H. Kruger Dr. T. Fessenden Dr. W. Barletta P.O. Box 808 Livermore, CA 94550	1 1 1 1	Science Applications, Inc. ATTN: Dr. M. P. Fricke 1200 Prospect Street P.O. Box 2351 La Jolla, CA 92038	1
Los Alamos National Laboratory Attn: Dr. G. Best Dr. H. Dogliani Dr. T. Starke P.O. Box 1663 Los Alamos, NM 87545	1 1 1	Science Applications, Inc. ATTN: Dr. R. Johnston 5 Palo Alto Square Palo Alto, CA 94304	1
Mission Research Corporation ATTN: Dr. C. Longmire P.O. Drawer 719 Santa Barbara, CA 93102	1	TRW ATTN: Dr. John Bayless One Space Park, R1/1078 Redondo Beach, CA 90278	1
Mission Research Corporation ATTN: Dr. B. Godfrey 1720 Randolph Road S.E. Albuquerque, NM 87106	1	Commander, Naval Surface Weapons Center ATTN: Mr. R. Biegalski, N13 Dr. R. Cawley, R41 Dr. M. Cha, R41 Dr. R. Fiorito, R41 Dr. J. Forbes, R13 Dr. C. Huddleston, R401 Dr. E. Nolting, F34 Dr. M. Rose, F04 Mr. R. A. Smith, F34 Dr. H. Uhm, R41 Library, X211 Silver Spring, MD 20910	1 1 1 1 1 1 1 1 1 1